scientific reports

Check for updates

OPEN

A novel approach for wine anti-counterfeiting using laser-induced graphene chipless RFID tags on cork

Antonio Lazaro[1]✉, Marco Rodrigo Cujilema[1], Ramon Villarino[1,2], Marc Lazaro[1,2] & David Girbau[1,2]

This work introduces novel, non-cloneable chipless RFID tags designed for authentication, offering a solution to protect product brands, such as wine, liquor, oil, and other liquid products, from counterfeit practices. A unique spectral response of the embedded tag, created by depositing various conductive layers, can be achieved by combining its shape and sheet resistance. To accomplish this, a laser-induced graphene (LIG) layer is formed on a cork substrate (used as a graphene precursor), followed by an electroplating process to enhance conductivity. This paper presents a prototype scanner, designed to characterize the electromagnetic signature of the tags, compatible variable-sized wine bottles and cork stoppers. Preliminary results obtained with complex logo images demonstrate the feasibility of this technology.

Keywords Radio identification, Laser-induced graphene (LIG), Chipless-RFID, Near-field, Non-cloneable tag, Authentication, Counterfeit, Cork

The rise of global trade via the internet has increased the issue of counterfeiting[1]. While offering unprecedented reach for genuine brands, online platforms also provide channels through which counterfeit products can easily enter the market. Several industries such as pharmaceuticals[2], wine[3,4], textiles[5,6] and oil[7] are significantly affected by this problem. The wine industry faces significant challenges due to counterfeit and adulterated products[8]. These fraudulent practices not only deceive consumers but also undermine the reputation and economic stability of authentic wine producers. Counterfeit wines often lack the quality and authenticity of genuine products, posing potential health risks and diminishing consumer confidence. Methods of protection include advanced technologies such as holograms, QR codes[9], and Radio Frequency Identification (RFID) tags[7]. Blockchain technology is increasingly being used to track the supply chain and verify product authenticity[10]. Companies also invest in secure packaging designs that are difficult to replicate[4].

The authenticity of an object goes beyond mere identification and must be verified. While conventional passive RFID has been proposed as an authentication solution[11,12], these tags are easily cloned. Various anti-counterfeit technologies are well-documented in the literature, including the use of fingerprints to develop physical non-cloneable functions (PUFs)[13]. Chipless RFID technology refers to a type of RFID that does not include microchips. Instead, information is encoded in its unique electromagnetic signature. Due to its potential low cost, this technology offers a promising solution for various applications, including anti-counterfeiting. By incorporating unique identifiers, chipless RFID can also help to verify the authenticity of products. Chipless tags based on dipoles and resonators have been proposed as non-cloneable tags[14,15], so that the multiple resonance frequencies are useful for identifying them. However, these structures are based on simple layouts. Another type of chipless tag involves inserting random wires into a dielectric sealant, creating an RF fingerprint[16]. Embedded resonators made with additive manufacturing have been recently proposed in[17,18]. Since non-standardized readers based on network analyzers are usually needed, reading these tags requires specialized equipment, which makes cloning them difficult.

Cork has been the preferred choice for sealing wine bottles for centuries[19]. This natural material, extracted from the bark of cork oak trees, provides an effective barrier to air, allowing the wine to age properly. Cork's elasticity and impermeability make it ideal for maintaining the wine's and liquor's integrity over time. This work

[1]Department of Electronics, Electrics and Automatic Control Engineering, Rovira i Virgili University, Tarragona 43007, Spain. [2]These authors contributed equally: Ramon Villarino, Marc Lazaro and David Girbau. ✉email: antonioramon.lazaro@urv.cat

proposes a method to embed a chipless tag on the cork stoppers for authentication. Logo images printed with conductive materials on the cork stopper can be used to create specific electromagnetic signatures measured by the reader. To this end, the traces on the cork are made using laser-induced graphene (LIG). LIG offers several notable advantages. Its relatively inexpensive and scalable manufacturing process makes it an attractive option for various applications. LIG boasts an excellent electrical conductivity that is crucial for the operation of electronic devices and sensors. Its porous structure enhances the surface area, making it ideal for energy storage devices such as supercapacitors and batteries[20]. Additionally, LIG is flexible and can be fabricated on different types of substrates, expanding its potential use in wearable technology and flexible electronics[21]. The eco-friendly production process of LIG, which often involves the use of biodegradable materials like cork[22], wood[23] or polyimide[18,24], also contributes to its appeal.

Laser-induced graphene (LIG) is increasingly being used in sensing applications due to its unique properties. LIG is a three-dimensional porous material created by laser scribing, which offers high electrical conductivity, excellent thermal stability, and a large surface area. These properties make LIG an ideal candidate for fabricating sensors that are sensitive, reliable, and capable of detecting a wide range of stimuli. LIG-based sensors have been successfully applied in fields such as environmental monitoring, healthcare, and wearable technology. For instance, LIG can be used to develop highly sensitive gas sensors, biosensors for medical diagnostics, and flexible strain sensors for wearable devices[25,26]. The simplicity and cost-effectiveness of the LIG fabrication process further enhance its appeal for widespread sensor applications[27].

System architecture

Figure 1 presents a block diagram of the system. The tag is composed of resonators engraved as a LIG image, printed directly with a CO_2 laser. The layout dimensions, shape, and materials determine the resonance frequencies and electromagnetic frequency response. LIG conductivity and thickness are influenced by the parameters used in the laser manufacturing process. Although the obtained conductivity is relatively high and suitable for many sensor applications, it is insufficient for resonators requiring high quality factors. Additionally, to introduce a higher degree of uncertainty and improve conductivity, a conductive layer of varying thickness is electroplated on top of the LIG[18]. The tag characterization is conducted using a custom-designed near-field scanner compatible with wine bottles.

A vector network analyzer is used to measure the transmission coefficient (parameter S_{21}) of a setup consisting of a microstrip line connected to two SMA launch connectors at its ends, which are connected to both ports of the VNA. The tag under test spins thanks to the action of a stepper motor, allowing the VNA to scan the electromagnetic response of tag. The measured S_{21} parameter for each tag is saved in a database for the subsequent application in the validation procedure. This validation involves performing the measurement using the same configuration and comparing the tag response with the stored in the database. In the event of a mismatch, the tag will be considered as a counterfeit.

Results and discussion

First, the feasibility of using cork as a precursor for graphene has been studied. There are different types of cork stoppers, each one suitable for each type of wine and aging processes[28]. Samples with different cork granule sizes have been investigated. Their pores are filled with a mixture of cork powder and glue. Type A cork is composed of smaller granules than the other types, while Type D has the largest granules (see Figure 2). Raman spectroscopy is a powerful tool for characterizing LIG material[29]. Figure 3 shows the measured Raman spectrum of different LIG samples performed the same duty cycle (12%) or average laser power (4.8W) and speed (24 mm/s) for different kinds of cork stoppers. Raman spectrum is measured with Renishaw's InVia confocal Raman microscope. The Raman spectrum of graphene is characterized by several key frequencies, each of which

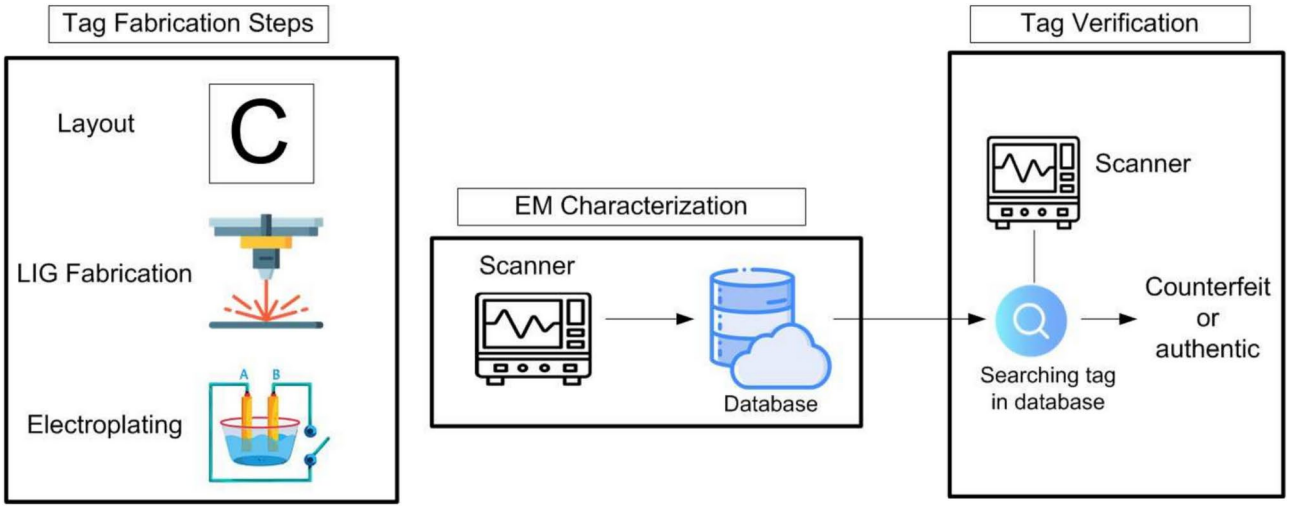

Fig. 1. Schema of the proposed authentication system.

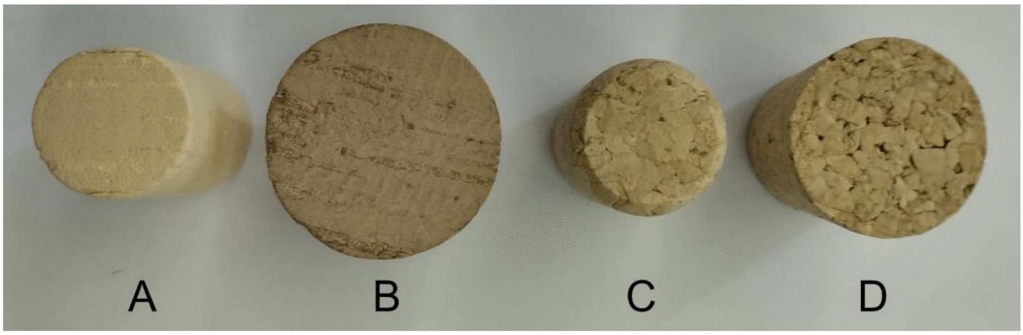

Fig. 2. Types of cork stoppers analyzed according to the different granule size.

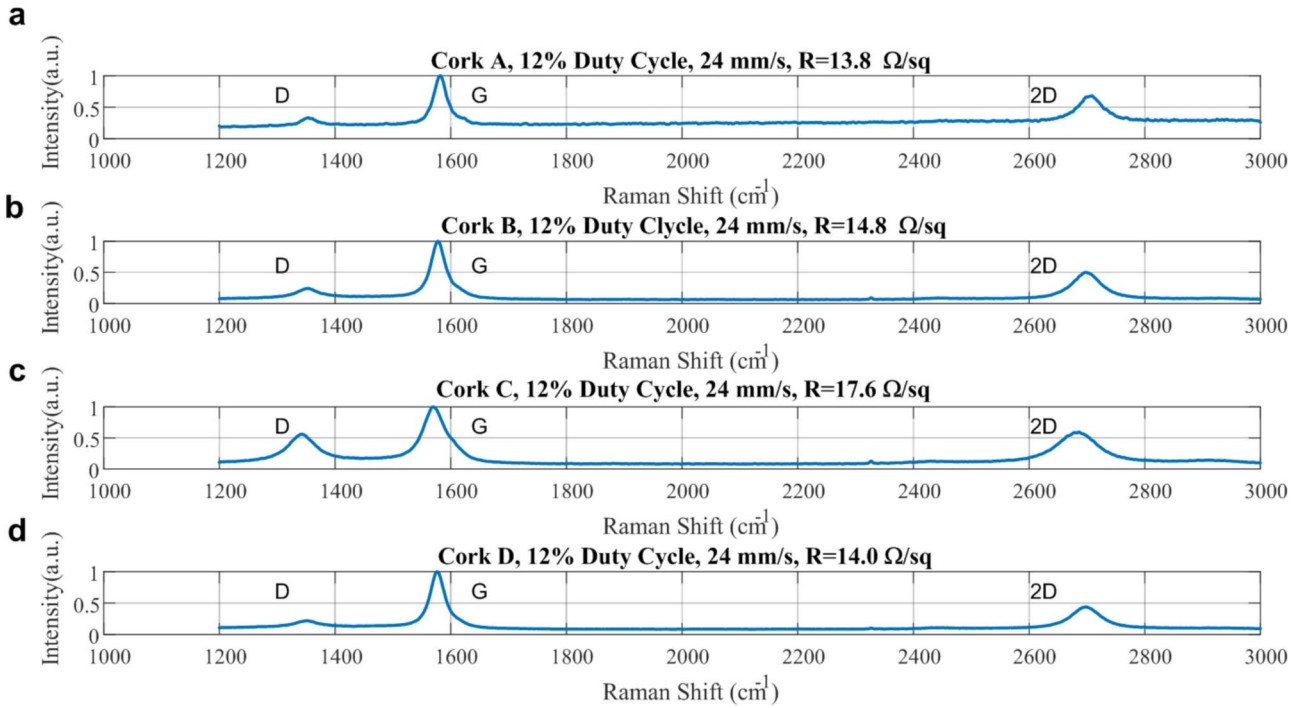

Fig. 3. Normalized Raman spectrum for different types of cork stoppers with similar sheet resistance, manufactured using a LASER with a 12% duty cycle, a speed of 24 mm/s, and a maximum power of 40 W. The characteristic peak at frequencies D, G, and 2D is observed: (**a**) Cork A, (**b**) Cork B, (**c**) Cork C, (**d**) Cork D.

provides information about its structure and properties, denoted as G, D, and 2D bands. G peak (1592 cm^{-1}) is the primary vibrational mode of graphene, D peak (1350 cm^{-1}) is often used as an indicator of the level of disorder or defects in the graphene, and 2D peak (2685 cm^{-1}) is sensitive to the number of graphene layers and provides information about the electronic structure. A high 2D peak value in LIG is an indicator of the presence of well-ordered, multilayer graphene structures which is beneficial for applications requiring high electrical conductivity and mechanical strength. The 2D/G ratio values obtained are within the range 0.4 to 0.6. On the other hand, D/G ratios of less than 0.5 were obtained in all samples, indicating the low presence of defects. In addition to Raman spectroscopy, other researchers have investigated the formation of LIG on cork[22] and other precursor materials[30] using X-ray photoelectron spectroscopy (XPS). This surface analysis technique has confirmed that the laser-irradiation process increases carbon concentration and reduces oxygen-containing functional groups. This change occurs due to the photothermal effect induced by the laser, which raises the temperature of the material and causes the atomic lattice to vibrate, breaking various C-O and C=O bonds. These bonds then recombine and are released in the form of gases (e.g., O_2, CO_2).

In some cork stoppers, test structures consisting of a strip 1 cm long and 2 mm wide are manufactured. The sheet resistance of samples with different LASER power is shown in Figure 4, in addition to the standard deviations for each of the cases for which three different samples were made. As the power increases, the sheet resistance decreases almost linearly. Once the thermal power exceeds approximately 4.8 W, an oxidation process begins, which causes a flattening of the slope, similar to what happens in the case of LIG on polyamide[29]. Samples

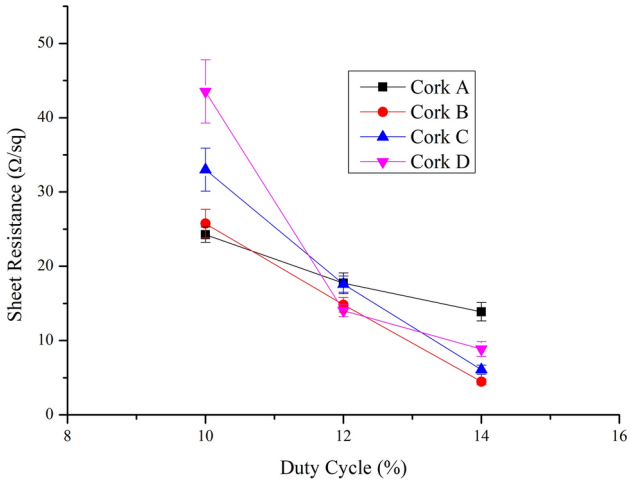

Fig. 4. Sheet resistance as a function of the duty cycle for different types of cork.

show a greater deviation in type D cork due to its larger grain size. As expected, higher laser power tends to increase porosity, as shown in the SEM images taken on the backsides of the LIG films.

A more comprehensive understanding of the LIG formation process on cork can be achieved using Scanning Electron Microscopy (SEM). The formation process of LIG on cork differs from that of polyimide. On polyimide, LIG is formed on the precursor surface, whereas on cork, it is etched into the material. After laser illumination, the cork structures break, forming visible stripes, as shown on the left side of Figure 5a. The width of these bands is about 50 μm, similar to the width of the laser beam. The distance between them is about 100 μm, coincident with the spacing between consecutive laser passes. The morphology of the graphene, detailed in Figure 5b, corresponds to that of a fibrous structure. This provides high conductivity due to the higher homogeneity of the formed surface, thanks to the use of medium laser power and low velocity. Figure 5c shows a cross-section in which the average thickness of the LIG layer is approximately 500 μm. The ordered multilayer structure of the graphene, as shown in Figure 5d, is clearly distinguishable from that of the cork.

To investigate the metallization on the LIG, SEM images are generated. Figure 6.a shows a top view of the nickel layer formed during electroplating for 900 seconds at a current of 23 mA, on a LIG layer fabricated at 12% duty cycle and 24 mm/s Figure 6.b reveals the presence of carbon (red) and nickel (blue) after performing energy-dispersive X-ray spectroscopic (EDS) analysis. The EDS spectrogram shown in Figure 6.c confirms that the LIG is almost completely covered by nickel. A transverse cut is shown in Figure 7. Figure 7.a shows the nickel layer embedded on the LIG. Figure 7.b shows the composition of carbon (red) and nickel (blue). It can be seen how the nickel gradually penetrates into the porous structure of the LIG. Figure 7.c shows the EDS spectrogram that confirms the presence of nickel.

To increase the quality factor of the resonators and facilitate their detection, the sheet resistance must be reduced. For this purpose, an electroplating layer of Nickel of thickness t_p is grown on the LIG[18]. Figure 8 shows the typical measured sheet resistance as a function of plating time. A 15 mm long and 4 mm wide LIG sheet engraved on type A cork is analyzed. The LIG sheet has an initial sheet resistance of 19 Ω/sq. An electroplating current of 23 mA was used to electroplate the Nickel. A change in slope is observed when the Nickel covers the porous LIG. Consequently, conductivity is modeled into two parts: the first takes into account the average conductivity of the LIG, the metal inside the porous LIG, and the gaps between the traces; the second considers the formation of a rough metal layer on the LIG. To model this behavior, an effective conductivity is considered:

$$\sigma(t_p) = \begin{cases} \frac{\sigma_{LIG} t_{LIG} + \sigma_1 \cdot t_p}{t_{LIG} + t_p} & , t_p \leq t_{th} \\ \frac{\sigma(t_{LIG})(t_{LIG} + t_{th}) + \sigma_2 \cdot (t_p - t_{th})}{t_{LIG} + t_p} & , t_p > t_{th} \end{cases} \quad (1)$$

where t_{LIG} is the thickness of the LIG, which is 500 μm; t_{th} is the threshold thickness for modeling the roughness and porosity of the LIG surface, which determines the instant where the slope in the sheet resistance changes (a value of 1.2 μm was considered); σ_{LIG} is the conductivity of the LIG (a value of 2500 S/m, measured from its DC sheet resistance, was obtained); σ_1 and σ_2 are the conductivities of the electroplated metal inside and on the LIG, respectively, and are considered fitting parameters. The values found were $\sigma_1 = 5.5 \cdot 10^6$ S/m and $\sigma_2 = 1.02 \cdot 10^7$ S/m, respectively. These values are lower than bulk nickel conductivity due to the porosity and roughness of the galvanized surface. The thickness t_p is obtained from the electroplating time determined by Faradays's law. The proposed conductivity model demonstrates good agreement between the measured and modeled sheet resistance (see Figure 8). Therefore, by controlling the electroplating time, it is possible to manage the sheet resistance, and indirectly, the quality factor of the resonators (see[18] for a model of microstrip ring resonators). This parameter introduces a degree of randomness that increases the variability of the tags, making them difficult to clone or counterfeit.

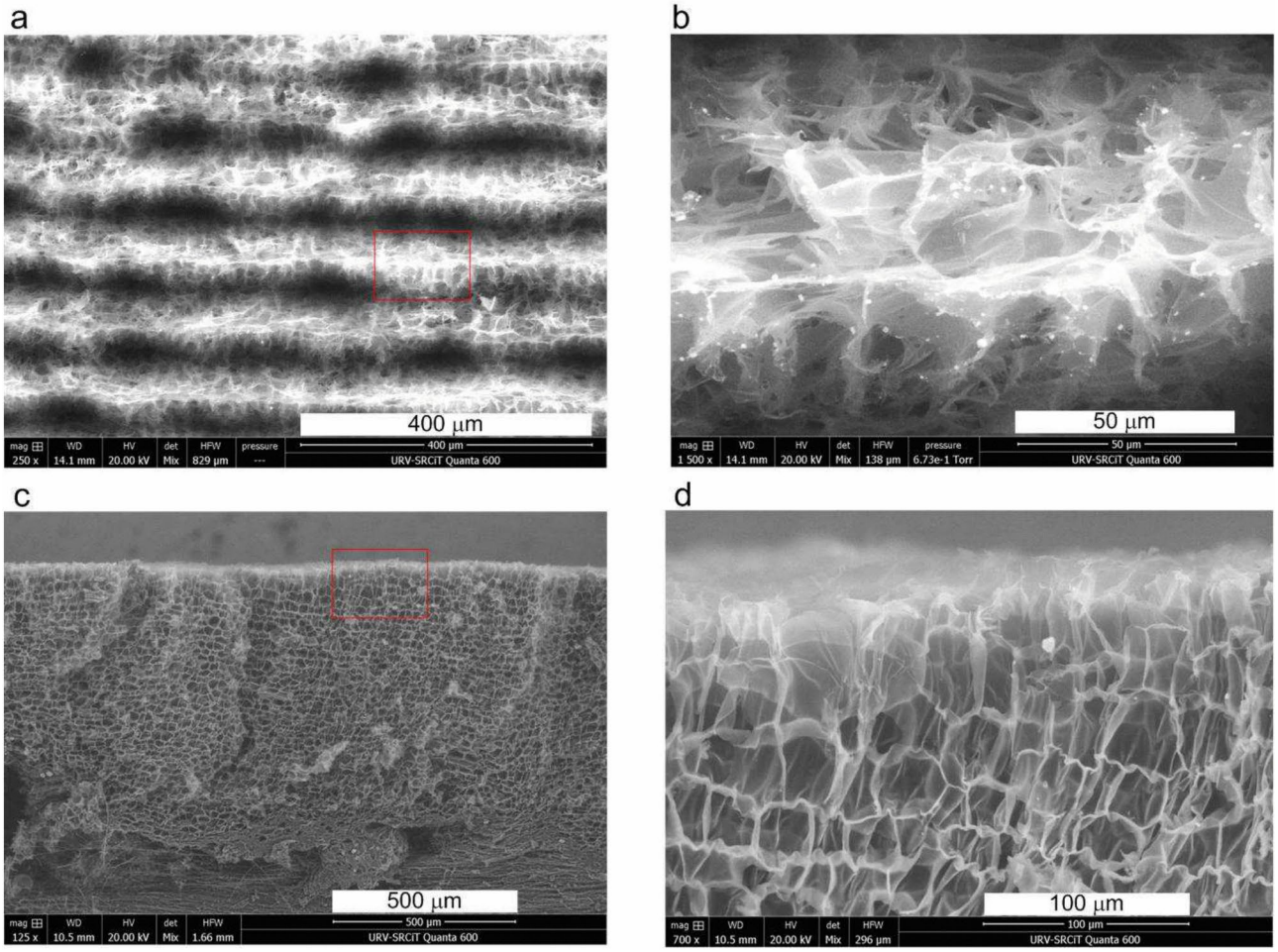

Fig. 5. SEM images of cork type A fabricated at 12% duty cycle and 24 mm/s: (**a**) top view showing the stripes due to consecutive laser passes, (**b**) zoom of top view where fibrous morphology of LIG is observed, (**c**) cross-section of the ordered multilayer structure of graphene once it penetrates the cork. Its thickness is about 500 μm within the cork, (**d**) zoom of the area delimited by the red rectangle in (**c**).

Figure 9 shows the measured transmission parameter (S_{21}) of some tags as a function of the frequency between 100 MHz and 12 GHz, at different angular positions. The tags are cork stoppers with various layouts (A, F, P characters) or the logo of the New York Yankees as an example of a more complex design; however, arbitrary images can also be printed using the laser engraver. A power of 4.8 W and 24 mm/s were used. After that, the tags are electroplated with Nickel. A microstrip line measurement is conducted without the tag (background), which serves as a reference to correct the microstrip line losses, thereby enhancing the resonances. The randomness in the electromagnetic signature as a function of the angle is evident.

To classify the tags, a method based on the calculation of the root mean square error of the spectral response is applied. Root mean square (RMS) error between the measured S_{21} parameter, in dB, of two resonators *i* and *j* ($RMS(i,j)$) can be computed using the following expression:

$$RMS(i,j) = \sqrt{\frac{1}{N_a}\sum_{k=1}^{k=N_a}\frac{1}{N}\sum_{n=1}^{n=N}|20log(|S_{21i}(n)|) - 20log(|S_{21k}(n)|)|^2} \quad (2)$$

where N and N_a denote the number of measured frequencies and angular positions, respectively. Table 1 shows the computed error between pairs of tags of Figure 9. The average of 5 measurements is shown, The tag is identified if the RMS error is less than a threshold fixed at $3 \cdot 10^{-2}$ dB (three times the difference between the same tag) since the uncertainty in the VNA measurement must be taken into account. Table 1 shows that the tags are distinguishable between them.

To investigate the effect of conductivity on the electromagnetic signature, three tags with the shape of F character but with different electroplating times (100 s, 200 s, and 900 s) have been fabricated (see Figure 10a). The corrected S_{21} measurements of the tags are shown in Figure 10a–d. No resonances are observed in tags with excessively short due to high conductor losses. However, the results in Figure 10c–d show, respectively for

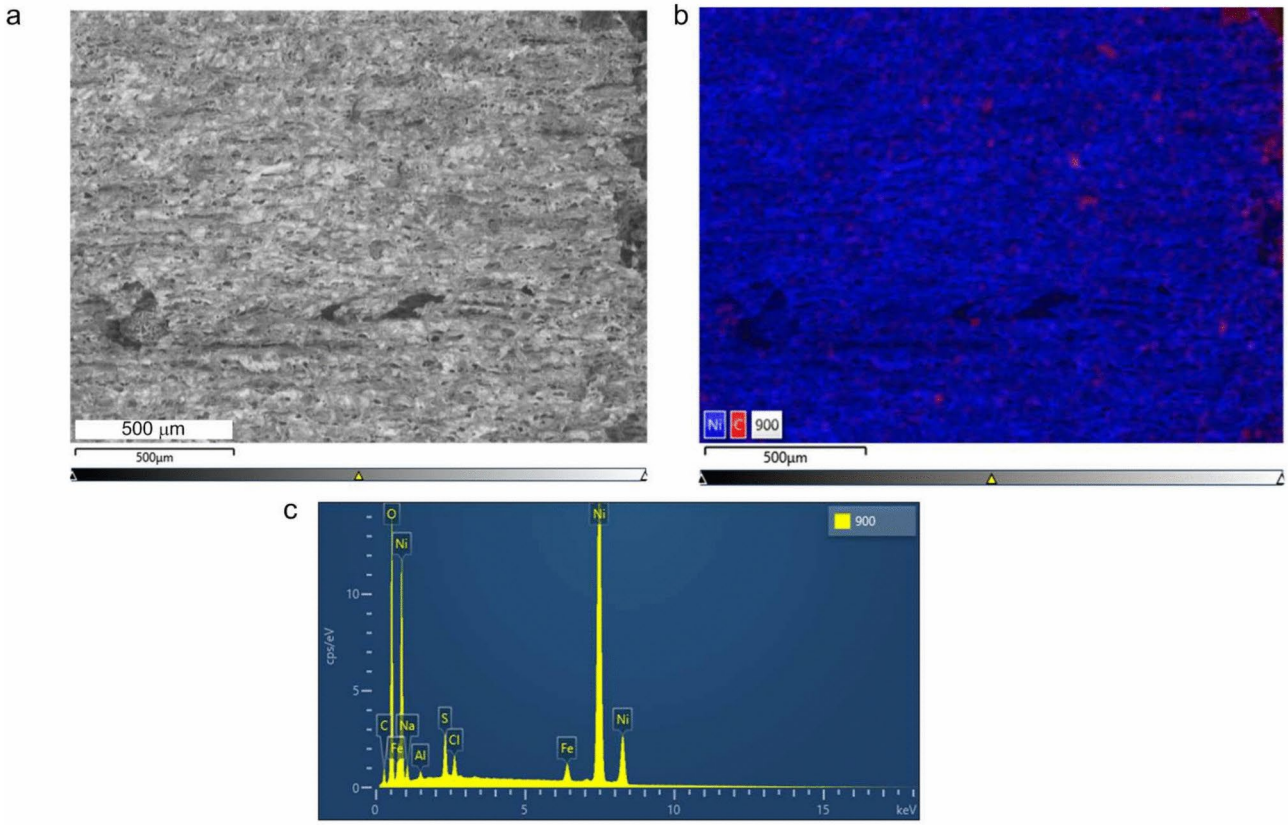

Fig. 6. SEM images of type A cork fabricated with a duty cycle of 12% and 24 mm/s, and an electroplating time of 900 s with a current of 23 mA: (**a**) top view showing stripes covered by Nickel, (**b**) top view showing the composition (blue Nickel and red Carbon), (**c**) EDS Spectrogram.

electroplating times of 200 and 900 seconds, the resonances detected in the 4 to 6 GHz band and their harmonics in the 10 to 12 GHz band, the latter due to its better conductivity. Table 2 shows the RMS error values between tags depending on the exposure times, highlighting clear differences. It can be concluded that even with the same layout and type of cork, different responses can be achieved by controlling the electroplating time, thus protecting the tags from possible cloning.

To investigate the effect of laser parameters on the tags, Figure 11 shows three tags the letter "F" engraved on them, made at a speed of 24 mm/s but with different duty cycles (10%, 12%, and 14%) and the same electroplating time (900 s at 23 mA). The response is distinguishable due to variations in the final quality factor of the resonances, which are influenced by the different conductivity and thickness of the layers obtained. In Figure 11c and d, the resonance at high frequency (9-12 GHz) is detectable, whereas it is difficult to detect in Figure 11b due to higher losses produced for low duty cycles. For the 14% duty cycle, the width of the traces is slightly higher due to the excess power, which begins to partially burn the cork. Table 3 compares the RMS error of the measured S_{21} between the tags, showing that they are clearly distinguishable.

Figure 12 shows the RMS error between 15 tags manufactured with the same parameters, with respect to one of them taken as a reference. The tag is engraved with the character F and the parameters used were: laser power and speed of 4.8 W and 24 mm/s respectively, electroplating performed for 900 s, with a current of 20 mA. Results show that the repeatability is less than 0.07 dB. This value is the result of a combination of deviations caused by the manufacturing process, as well as the measurement error of the network analyzer (estimated in 0.01 dB). During the verification process, the tag must be placed in the same position and orientation as when the EM signature was recorded in the database. Alignment is achieved with a simple, purpose-designed holder for the bottle. A reference mark on the bottle can be used as an angular alignment tool. In order to study the sensitivity to angular misalignment, the mean square error (see Figure 13) has been calculated, observing that it is minimized the better aligned the tag is. Therefore, angular errors of ± 30 degrees can be corrected by simply shifting the measurement matrix and searching the angular position that minimizes the RMS error.

Although wine bottle stoppers are coated with a protective plastic, to avoid damaging the LIG surface and the electroplated layer, an additional protective layer can be added. For example, resins or lacquers can be used, even incorporating dyes to darken the tag design and make it more difficult to copy. Additionally, PVA-based glue or other adhesive can be added, which would cause the tag to break when the protective plastic is removed. Since these thin dielectric layers have low permittivity (around 2-3), they would only cause shifts at resonance frequencies, introducing even more randomness.

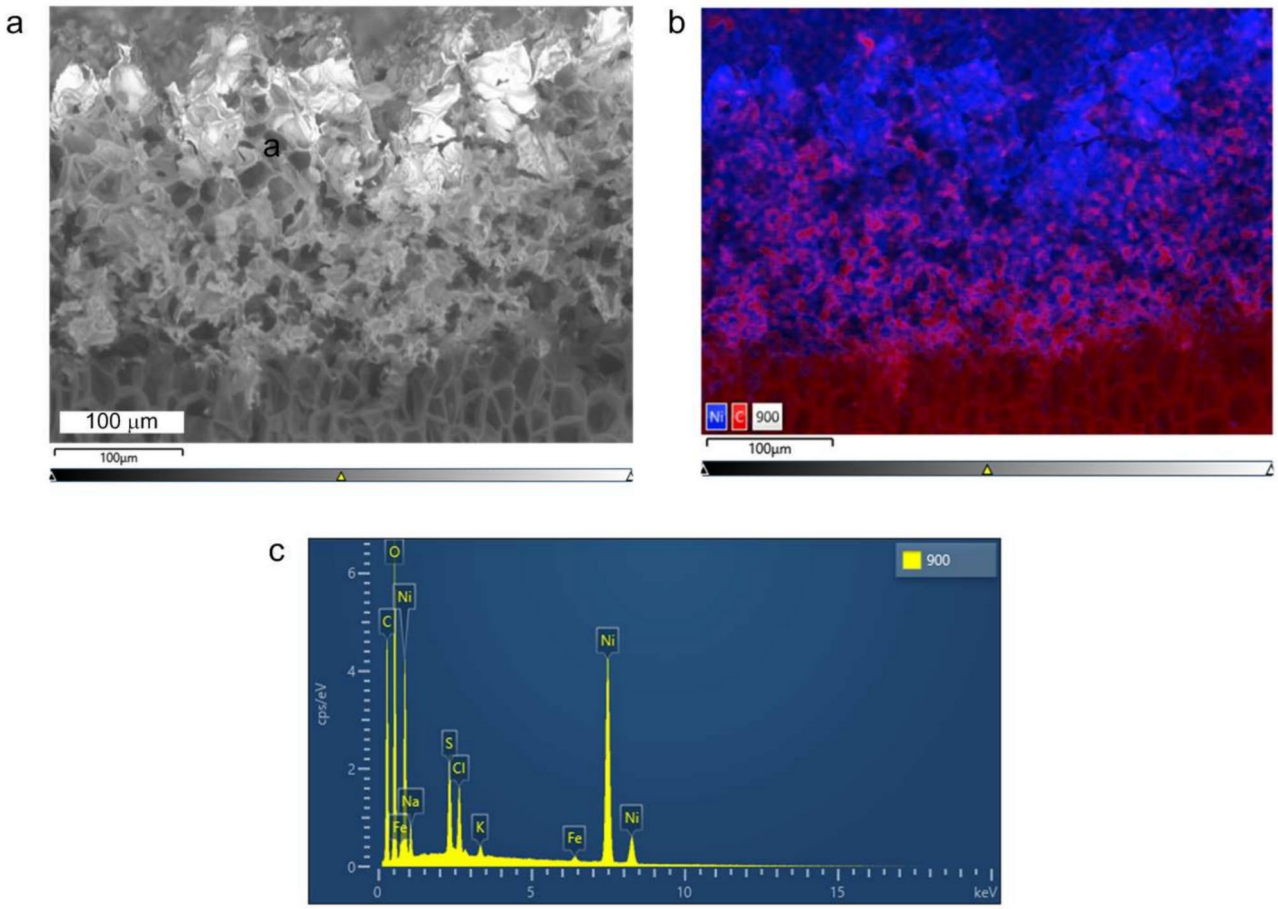

Fig. 7. SEM images of type A cork fabricated with a duty cycle of 12% and 24 mm/s, and an electroplating time of 900 s with a current of 23 mA: (**a**) cross-section of the interface corresponding to the ordered multilayer structure of graphene and nickel layer, (**b**) cross-section showing the composition (blue Nickel and red Carbon), (**c**) EDS Spectrogram.

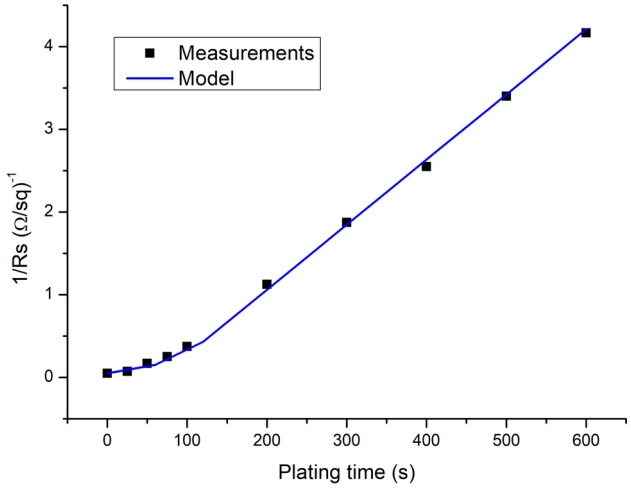

Fig. 8. Comparison of the measured and modeled sheet resistance as a function of plating time.

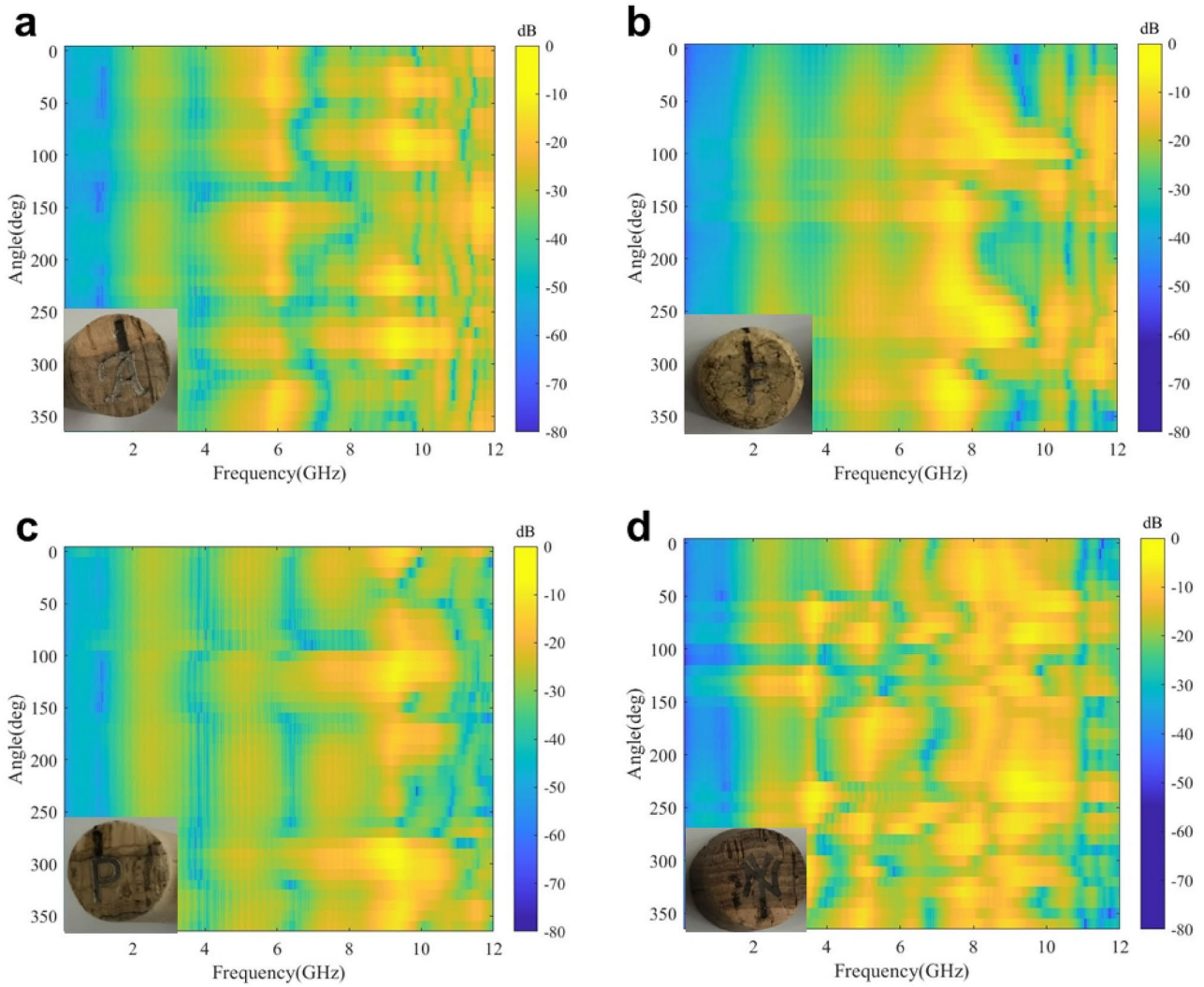

Fig. 9. Corrected S_{21} measurements of four different tags as a function of the frequency and angular position: (**a**) Character A, (**b**) Character F, (**c**) Character P, and (**d**) Logo NY.

Tag	a	b	c	d
a	0.01	1.18	0.63	1.76
b	1.18	0.01	1.24	1.78
c	0.63	1.24	0.01	1.75
d	1.76	1.78	1.75	0.01

Table 1. Root mean square (RMS) error of the measured S_{21} between tags shown in Figure 9.

Conclusions

A novel method for the design of unclonable tags for wine anti-counterfeiting applications, based on the measurement of electromagnetic spectral signatures in the near-field has been proposed. The tags have been fabricated using laser-induced graphene (LIG) on cork stoppers, designed to exhibit random resonance frequencies. An electroplating process has been implemented to vary the quality factor of the resonators. The large number of manufacturing parameters provides an additional level of security, which adds to the inherent manufacturing imperfections to prevent tag cloning. A scanner, based on a microstrip line that rotates around itself very close to the tag, thanks to the action of a stepper motor, allows the transmission coefficient to be measured by means of a VNA operating in scalar mode (only magnitude information is used). The experimental results are highly promising, demonstrating the feasibility of this technology for anti-fraud detection in brand protection.

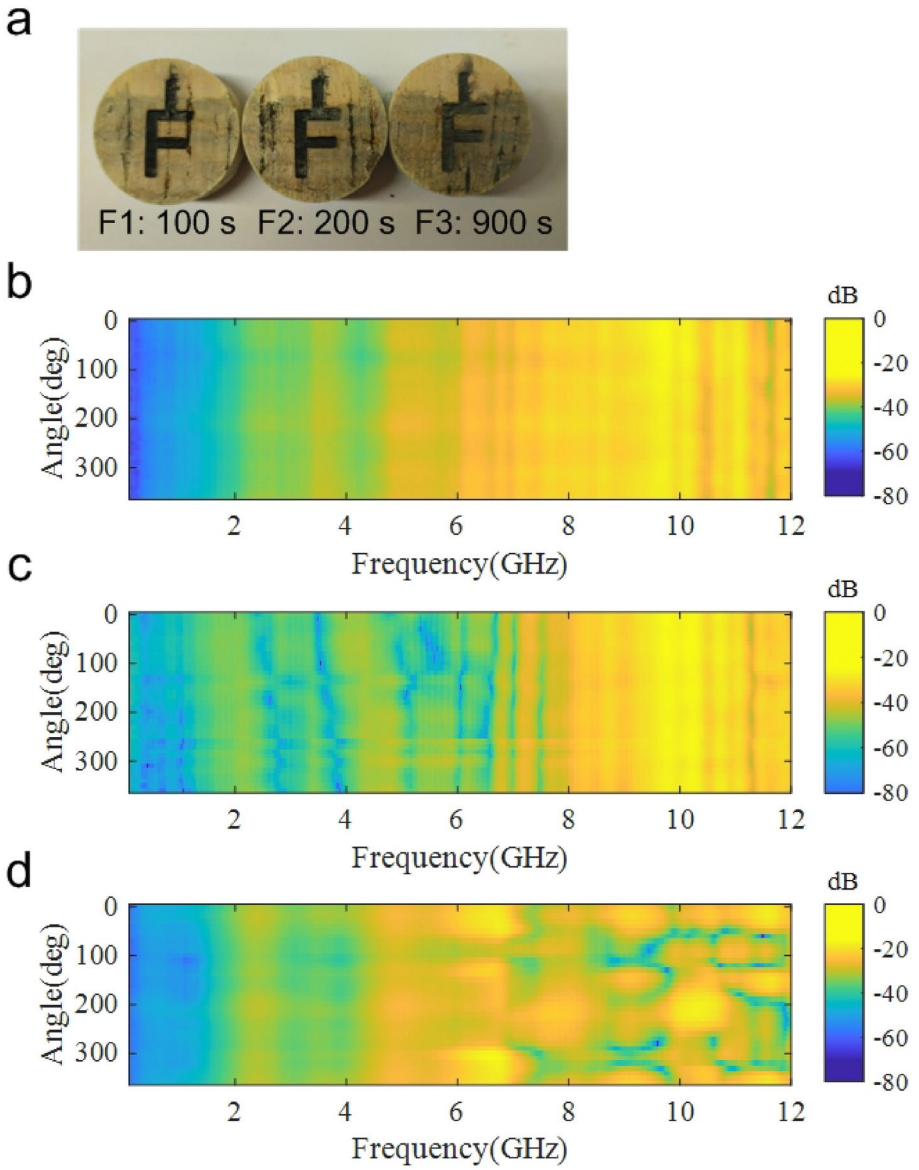

Fig. 10. (**a**) Image of tags printed with the character F and manufactured with electroplating times of 100 s, 200 s, and 900 s. (**b**)-(**d**) Corrected S_{21} measurements of the tags as a function of frequency and angular position, corresponding to electroplating times of 100 s, 200 s, and 900 s, respectively.

Tag	F1	F2	F3
F1	0.01	0.17	0.37
F2	0.17	0.01	0.37
F3	0.37	0.37	0.01

Table 2. Root mean square (RMS) error of the measured S_{21} between tags shown in Figure 10.

Methods

Materials

A commercial sheet of natural agglomerated cork was purchased from AR Estrategias (Badajoz, Spain) and used without any treatment or adding any fire retardant. In addition, cylindrical natural cork stoppers sealed with cork powder and water-based glue of different grain sizes were acquired.

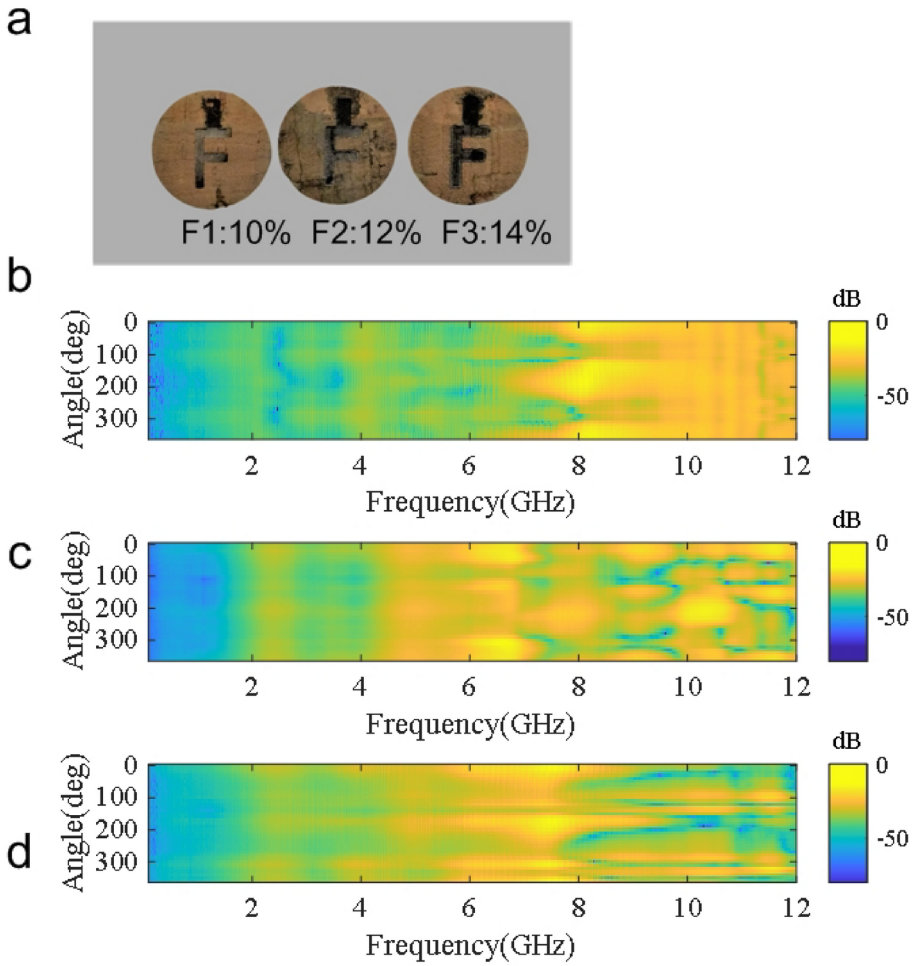

Fig. 11. (**a**) Image of the manufactured tags (letter F). The LIG layer was generated by applying the following laser power levels respectively: 10%, 12% and 14%, (**b**)-(**d**). The electroplating time was 900 s. (**b**)-(**d**) Corrected S_{21} measurements of the tags as a function of frequency and angular position for the three cases mentioned above.

Tag	F1	F2	F3
F1	0.01	0.27	0.37
F2	0.27	0.01	0.34
F3	0.37	0.34	0.01

Table 3. Root mean square (RMS) error of the measured S_{21} between tags shown in Figure 11.

Tag fabrication using LIG on cork susbtrate

Manufacturing utilizes a FLUX Beambox 40W (Kontich, Belgium) CO_2 laser engraver and cutter with a wavelength of 10.6 μm and a maximum power of 40 W. The laser source operates with pulse width modulation (PWM). Therefore, the average laser power irradiating the sample is the product of the maximum power and the duty cycle used. The resolution of the laser is 1000 dpi and its beamwidth is 50 μm. The conductivity and morphology of the LIG is a complex function dependent on laser parameters such as the duty cycle (or equivalently the average laser power), and the scan speed[31].The LIG on the cork sheet is produced at a specific irradiation energy threshold of the laser, at which point the conductive graphene-derived material begins to form[22]. In this work, the laser beam is scanned over the cork substrate at a speed of 20-24 mm/s, and with a duty cycle of 10-14%. The combustion of cork occurs at average power levels above the aforementioned value, within the range of scan speeds used.

Electroplating

To introduce a certain randomness by improving the quality factor of the resonance, the LIG samples are subjected to a nickel electroplating process. The previously LIG-patterned parts are connected to the cathode,

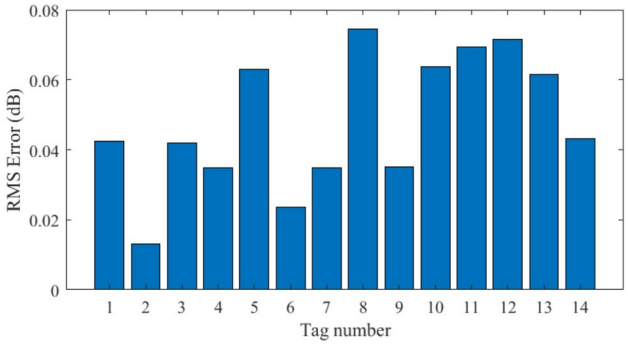

Fig. 12. Root mean square (RMS) error as a function of tag number. All tags printed with the character F and manufactured with the same parameters (12% duty cycle, 24 mm/s and 900 s of electroplating time).

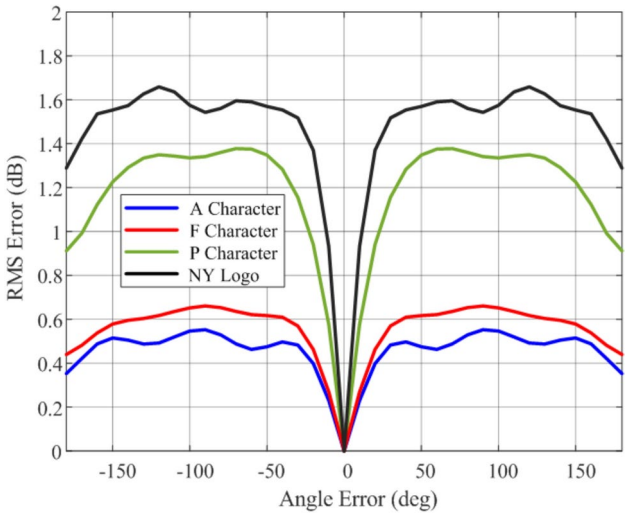

Fig. 13. Root mean square (RMS) error as a function of angle misalignment of the tags in Figure 9.

while a nickel rod is used as the anode. The electrolyte used is a nickel salt solution, specifically the nickel-plating solution from MARAWE GmbH & Co. KG (Regensburg, Germany), which contains nickel sulfate. The currents flowing through the solution in the electroplating process are within the range between 20 mA and 40 mA, driven by a DC power source (Agilent E3632A model) configured as a current source to limit the current level. Since the conductivity of laser-induced porous graphene is relatively low (reported values range from 200 to 2500 S/m[29]), the effective conductivity of the embedded resonators is mainly due to the high conductivity of nickel ($1.43 \cdot 10^7$ S/m). Nickel begins to infiltrate the porous structure of the graphene, gradually coating the entire surface. As the nickel layer covers the surface, its thickness increases, leading to a faster decrease of the sheet resistance. In fact, Faraday's law allows precise control over the thickness of the electrodeposited metal t_p, directly impacting the sheet resistance, by adjusting the plating time and current[32]:

$$t_p = \frac{I \cdot T \cdot M}{n \cdot F \cdot \rho_m \cdot A} \tag{3}$$

where T is the electroplating time, I is the electrical current, M is the molar mass of the plating metal (in grams per mole, 58.69 g/mol for Nickel), n is the number of electrons involved in the electrochemical reaction (valence number), F is the Faraday's constant (96485 C/mol), ρ_m the mass density of the plating metal (8.90 g/m^3 for Nickel), and A is the area of the electrode being plated. After the desired thickness of the metal coating is achieved, the cork stopper is removed from the electrolyte bath, rinsed, and dried.

Material characterization

The surface morphology was studied using the Environmental Scanning Electron Microscopy (ESEM) technique by means a Quanta 600 instrument from FEI Company (Hillsboro, Oregon, USA). Raman spectrometer analyses were carried out by a confocal Raman microscopy inVia from Renishaw (Wotton-under-Edge, UK), using a Laser diode of 514 nm as excitation source. Sheet resistance measurements have been performed with 4 probes with an Agilent 34450A multimeter.

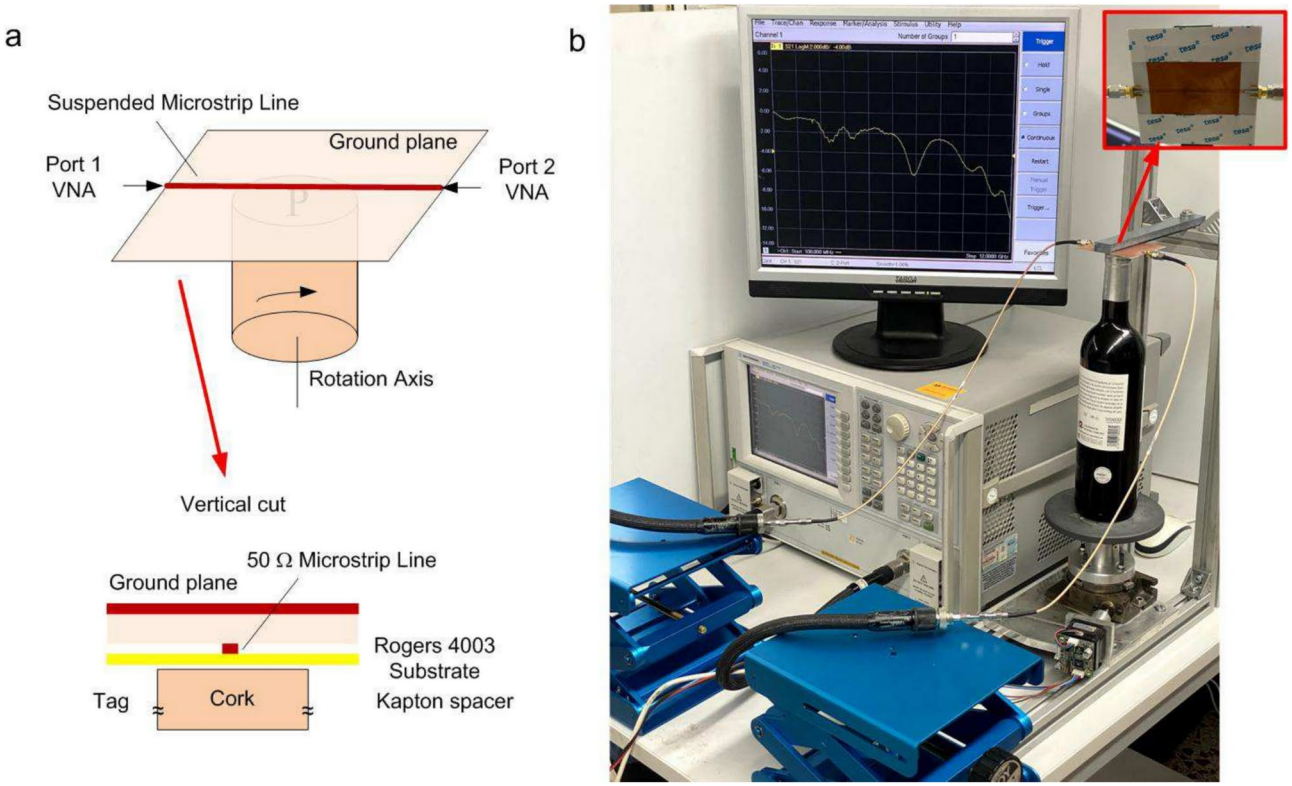

Fig. 14. (**a**) Schema of the scanner based on a suspended microstrip line over the tag (left) and a section view (right). The bottle, with the tag on the top, is placed on a rotary table controlled by a stepper motor that rotates it with precision. The transmission line connected to the VNA and printed on a substrate is covered with a KAPTON foil that acts as a protector to prevent the electrical contact when is approached to the tag engraved on the bottle stopper. (**b**) Photography of the experimental setup.

RFID reader measurements and data processing

To characterize the electromagnetic signature of the tags on wine bottles, a near-field reader has been specifically designed. It consists of a suspended microstrip line placed on the cork stopper. The bottle is supported on a rotary table controlled by a stepper motor with a reduction gear, allowing precise rotation. The microstrip line is a 50 Ω transmission line connected to both VNA ports (Agilent PNA E8364C). The thicknesses of the substrate (Rogers RO4003C) and its metallization, on which the line is manufactured, are 406 and 34 *mum*, respectively. A 75 μm Kapton sheet is used as a spacer between the line and the tag to ensure a constant gap, also avoiding electrical contact. The spacing between the suspended microstrip line and the rotary table can be adjusted depending on the height of the bottle. The bottle orientation is adjusted thanks to a mark printed on the tag. The VNA measures the transmission coefficient (S_{21} parameter) for each angular position. The sequence of the experiments performed consisted in performing measurements by moving the table in 10-degree steps, taking simultaneously 1601 points in the frequency range from 100 MHz to 12 GHz. Only the magnitude of S_{21} is required, so a scalar system (e.g., spectrum analyzer with tracking generator) could be used to reduce system costs. The S_{21} frequency response drops when the transmission line passes through a position that is coupled to a resonator. If the measuring frequency range is extended, multiple harmonics of the resonances can be observed. The depth and bandwidth of absorption observed at the resonant frequency depend on the quality factor, which is influenced by the material substrate and conductor losses[33]. Resonance frequencies are linked to the shape and size of the printed layout. In this work, due to the relatively low conductivity, the quality factor is primarily influenced by conductor losses due to the skin effect. Figure 14 shows a schematic and a photograph of the experimental setup, respectively. A video of the experimental setup is provided in the supplementary material.

Data availability

The data are available upon request to the corresponding author.

Received: 9 November 2024; Accepted: 7 April 2025
Published online: 13 April 2025

References

1. Jordan, F. & Kutter, M. Identifying counterfeit medicines with industry-suitable technologies. *Pharmaceutical Engineering, The Offical Magazine of ISPE* **32** (2012).
2. Al-Worafi, Y. M. Counterfeit medications in the developing countries. In *Handbook of Medical and Health Sciences in Developing Countries: Education, Practice, and Research*, 1–20 (Springer, 2023).
3. Costa, V., Sousa, A. & Reis, A. Preventing wine counterfeiting by individual cork stopper recognition using image processing technologies. *J. Imaging.* **4**, 54 (2018).
4. Soon, J. M. & Manning, L. Developing anti-counterfeiting measures: The role of smart packaging. *Food Res Int.* **123**, 135–143 (2019).
5. Yan, H. & Siesler, H. W. Identification of textiles by handheld near infrared spectroscopy: Protecting customers against product counterfeiting. *J. Near Infrared Spectrosc.* **26**, 311–321 (2018).
6. Agrawal, T. K., Koehl, L. & Campagne, C. A secured tag for implementation of traceability in textile and clothing supply chain. *Int. J. Adv. Manuf. Technol.* **99**, 2563–2577 (2018).
7. Maritano, V. et al. Anti-counterfeiting and fraud mitigation solutions for high-value food products. *J. Food Prot.* 100251 (2024).
8. Lecat, B., Brouard, J. & Chapuis, C. Fraud and counterfeit wines in France: an overview and perspectives. *Br Food J.* **119**, 84–104 (2017).
9. Popović, T. et al. A novel solution for counterfeit prevention in the wine industry based on iot, smart tags, and crowd-sourced information. *Internet of Things*. **14**, 100375 (2021).
10. Yiu, N. C. Decentralizing supply chain anti-counterfeiting and traceability systems using blockchain technology. *Future Internet*. **13**, 84 (2021).
11. Yiu, N. C. An nfc-enabled anti-counterfeiting system for wine industry. arXiv preprint arXiv:1601.06372 (2016).
12. Yao, W., Chu, C.-H. & Li, Z. The use of RFID in healthcare: Benefits and barriers. In *2010 IEEE International Conference on RFID-Technology and Applications*, 128–134 (IEEE, 2010).
13. Pappu, R., Recht, B., Taylor, J. & Gershenfeld, N. Physical one-way functions. *Science*. **297**, 2026–2030 (2002).
14. Deepu, V., Vena, A., Perret, E. & Tedjini, S. New RF identification technology for secure applications. In *2010 IEEE International Conference on RFID-Technology and Applications*. 159–163, https://doi.org/10.1109/RFID-TA.2010.5529879 (2010).
15. Yang, K., Forte, D. & Tehranipoor, M. M. UCR: An unclonable chipless RFID tag. In *2016 IEEE International Symposium on Hardware Oriented Security and Trust (HOST)*, 7–12 (IEEE, 2016).
16. DeJean, G. et al. RFDNA: A wireless authentication system on flexible substrates. In *2011 IEEE 61st Electronic Components and Technology Conference (ECTC)*, 1332–1337 (IEEE, 2011).
17. Genovesi, S., Choudhury, S., Gharibi, A., Costa, F. & Manara, G. Additive Manufacturing Technologies for Wireless Anti-Counterfeiting Solutions. In *2023 IEEE 13th International Conference on RFID Technology and Applications (RFID-TA)*, 130–133 (IEEE, 2023).
18. Lazaro, A. *et al.* Laser-induced graphene rf tags for authentication applications. *IEEE Access.* 1–1, https://doi.org/10.1109/ACCESS.2024.3489801 (2024).
19. Gil, L. *Cork composites: A review. Materials* **2**, 776–789. https://doi.org/10.3390/ma2030776 (2009).
20. Huang, L., Su, J., Song, Y. & Ye, R. Laser-induced graphene: En route to smart sensing. *Nano-micro letters.* **12**, 1–17 (2020).
21. Thaweeskulchai, T., Sakdaphetsiri, K. & Schulte, A. Ten. years of laser-induced graphene: impact and future prospect on biomedical, healthcare, and wearable technology. *Mikrochim. Acta* **191**, 1–30 (2024).
22. Houeix, Y. et al. Responsible humidity sensor by direct laser writing on cork substrate. *Adv. Sustain. Syst.* 2300606 (2024).
23. Ye, R. et al. Laser-induced graphene formation on wood. *Adv. Mater.* **29**, 1702211 (2017).
24. Romero, F. J. et al. In-depth study of laser diode ablation of kapton polyimide for flexible conductive substrates. *Nanomaterials.* **8**, 517. https://doi.org/10.3390/nano8070517 (2018).
25. Liu, J., Wu, D., Liu, C., Wang, Q. & Wang, H. Full-range on-body strain sensor of laser-induced graphene embedded in thermoplastic elastomer via hot pressing transfer for monitoring of the physiological signals. *Adv. Mater. Technol.* **9**, 2301658. https://doi.org/10.1002/admt.202301658 (2024).
26. Hu, X. et al. A comprehensive review of laser-induced-graphene for sensor applications: fabrication, properties, and performance evaluation. *J. Mater. Chem. C* - https://doi.org/10.1039/D4TC03547J (2025).
27. Liu, J. et al. Laser-induced graphene (lig)-driven medical sensors for health monitoring and diseases diagnosis. *Microchimica Acta*. **189**, 1–14. https://doi.org/10.1007/s00604-021-05157-6 (2022).
28. Díaz-Maroto, M. C. *et al.* Evaluation of the storage conditions and type of cork stopper on the quality of bottled white wines. *Molecules*. **26**, https://doi.org/10.3390/molecules26010232 (2021).
29. Lin, J. et al. Laser-induced porous graphene films from commercial polymers. *Nat. Commun.*. **5**, 5714 (2014).
30. Houeix, Y. et al. Laser-synthesis of conductive carbon-based materials from two flexible commercial substrates: A comparison. *Appl. Surf. Sci.* **634**, 157629. https://doi.org/10.1016/j.apsusc.2023.157629 (2023).
31. Duy, L. X. et al. Laser-induced graphene fibers. *Carbon*. **126**, 472–479. https://doi.org/10.1016/j.carbon.2017.10.036 (2018).
32. Wilcox, G. & Gabe, D. Faraday's Laws of Electrolysis. *Transactions of the IMF* **70**, 93–94. https://doi.org/10.1080/00202967.1992.11870951 (1992).
33. Pozar, D. M. *Microwave engineering: theory and techniques* (John Wiley & Sons, Singapore, 2021).

Acknowledgements

This research was funded by the projects PID2021-122399OB-I00 MICIU/AEI/10.13039/501100011033/FEDER, UE, and TED2021-130307B-I00 MICIU/AEI/10.13039/501100011033/ European Union NextGenerationEU/PRTR, and the grants PRE2019-089028 and PRE2022-103744.

Author contributions

A.L. conceived the experiments, A.L. and M.C. conducted the experiments and analyzed the results; M.C. fabricated the devices; R.V. and M.L. designed the experimental setup and A.L. drafted the main manuscript. All authors reviewed the manuscript.

Declarations

Competing interests

The authors declare no competing interests.

Additional information

Supplementary Information The online version contains supplementary material available at https://doi.org/1

0.1038/s41598-025-97613-z.

Correspondence and requests for materials should be addressed to A.L.